

Disposable Plasmonics: Plastic Templated Plasmonic Metamaterials with Tunable Chirality

Affar S. Karimullah,* Calum Jack, Ryan Tullius, Vincent M. Rotello, Graeme Cooke, Nikolaj Gadegaard,* Laurence D. Barron, and Malcolm Kadodwala*

Artificially engineered plasmonic metamaterials can manipulate light in unique ways affording new opportunities in optics and for spectroscopic detection and characterization of matter.^[1–5] These plasmonic phenomena can be exploited to create new sensing, data storage and photovoltaic technologies.^[6–10] With improved understanding of plasmonic phenomena, nanostructures with complex form factors can be designed for specific applications.^[5,11–13] To date the tuning of optical properties of metamaterials has been achieved through the design of the shape and symmetry of the constituent nanostructures. This form-factor driven manipulation of optical functionality is inherently limited in versatility since there is no scope for post-fabrication tuning of properties unless complex ferroelectric/magnetic/molecular materials are incorporated.^[14,15] Thus, tailoring optical properties using geometric design parameters and with low-throughput lithographic fabrication methods is both time consuming and expensive.

Here, we present a novel material, a continuous plasmonic metafilm consisting of periodic arrays of chiral nanostructures with optical properties that are significantly dependent on film thickness. These metafilms are grown on nanoindebited polycarbonate substrates which are fabricated using high-throughput injection molding, a technique used for Blu-Ray manufacturing. The cost effectiveness and reproducibility of injection molding provide advantages over nanoimprinting and e-beam fabrication.^[16–22] Thus these “templated plasmonic substrates” (TPS) offer low cost high-throughput fabrication,

effectively a disposable consumable, with properties which can be easily tuned in the production process.

The TPSs we generated can be considered to be hybrid structures, referred to as a solid-inverse structure, consisting of a solid nanostructure and an identical shaped void (inverse structure) directly above it. In line with Babinet's principle, the roles of electric and magnetic fields are switched between solid and inverse structures. The implications of this are that symmetry equivalent electric and magnetic modes of the solid and inverse structures are spatially located directly above each other, and can consequently couple in an analogous manner to hybridization of orbitals in molecular systems.^[23] We show with our chiral hybrid metafilms, that by controlling the spatial overlap between the solid and inverse structure, using film thickness, the coupling between electric and magnetic modes can be controlled enabling the chiral/optical properties to be manipulated with relative ease. This is a far more versatile approach to manipulating coupling in hybrid metamaterials than the current paradigm of altering the geometric design.^[24] Our work demonstrates that film thickness is an important parameter in the metamaterial design tool kit. To illustrate the potential of the tunable “disposable” TPS, we present an exemplar case where a chiral substrate, consisting of a periodic array of “shuriken” indentations which are either left (LH) or right handed (RH), is used for picogram characterization of protein structure with “plasmonic polarimetry.”^[5] The combination of the low cost injection-molded templates and the tunability of the films they can be used to produce, make the present study a significant step in the technological application of metamaterials.

The shuriken TPSs were fabricated using a new approach for templating Au films on nanostructured polycarbonate substrates. Injection molding enables high-throughput manufacturing of sub-micrometer resolution nanosurfaces with high levels of reproducibility and quality.^[21,25] In this work, we fabricate injection-molded polycarbonate templates, **Figure 1A**, that consists of chiral shuriken shaped indentations, of either left or right handedness, arranged in a square lattice. A detailed description of the injection-molding process can be found elsewhere.^[16,19,22,26] The depth of the indentation is 80 nm while the distance from the end of one arm to that of the end of the arm opposite is 500 nm. The periodicity of the array is 700 nm. Due to the nature of injection molding, the edges of the structure are not perfectly sharp and the inner walls of the structures are sloped by approximately 30° (see Supporting Information).

We deposited films of Au with thickness ranging from 20 to 100 nm on to the nanostructured polycarbonate template to produce the TPS samples, **Figure 1B,C**. The continuous nature of the Au films is evidenced by an absence of charging in scanning electron microscope (SEM) images of the substrates (see

Dr. A. S. Karimullah, C. Jack, R. Tullius,
Prof. G. Cooke, Prof. L. D. Barron,
Dr. M. Kadodwala
School of Chemistry
University of Glasgow
Joseph Black Building, Glasgow G12 8QQ, UK
E-mail: affar.karimullah@glasgow.ac.uk;
Malcolm.Kadodwala@glasgow.ac.uk

Prof. V. M. Rotello
Department of Chemistry
University of Massachusetts Amherst
710 Nt. Pleasant Street, MA 01003, USA

Prof. N. Gadegaard
School of Engineering
University of Glasgow
Rankine Building, Glasgow G12 8QQ, UK
E-mail: Nikolaj.Gadegaard@glasgow.ac.uk

This is an open access article under the terms of the Creative Commons Attribution License, which permits use, distribution and reproduction in any medium, provided the original work is properly cited.

The copyright line for this article was changed on 5 Nov 2015 after original online publication.



DOI: 10.1002/adma.201501816

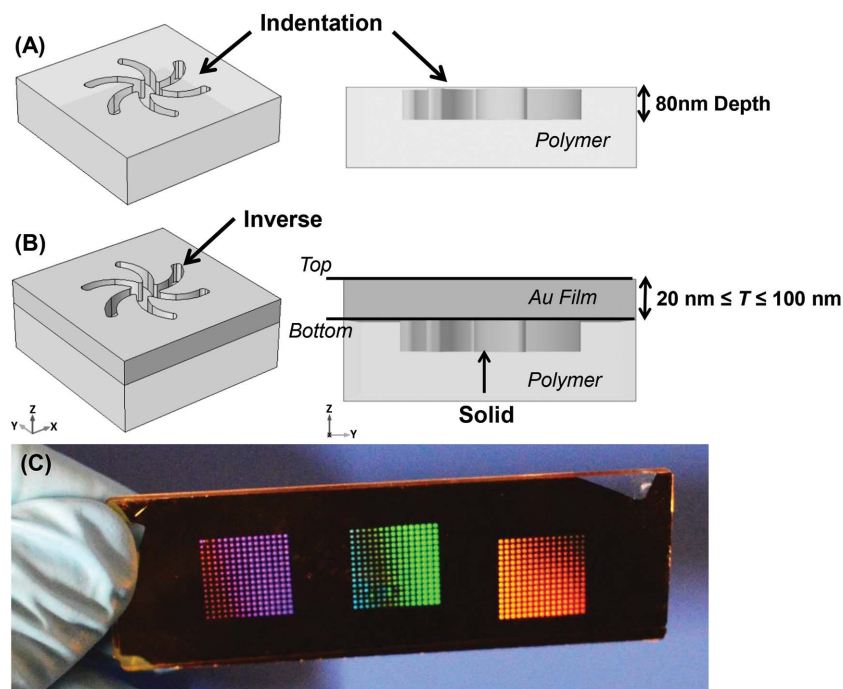


Figure 1. Hybrid plasmonic “shurikens”. Perspective and side views that show the geometry of a single structure, A) polymer substrate with an indentation that is 80 nm deep, B) a TPS is produced after depositing Au with a thickness (T) which is varied from 20 to 100 nm. The walls of the structure will always have a thin layer of gold hence a continuous film will be formed. The top of the structure is an inverse hole shape in the Au film and a solid nanostructure which is at the bottom. The top surface of the inverse structure is referred to as the “top surface” in the text and the top surface of the solid structure is called the “bottom surface.” C) The final TPS which is of the size of a typical microscope slide with multiple arrays of the nanostructures.

the Supporting Information). A continuous film is also an essential assumption for our EM models to reproduce experimental optical spectra (see the Supporting Information). To aid subsequent discussion we have defined two distinct surfaces of the TPSs. The “top surface” of the TPS contains the shuriken shaped voids, while the shuriken shaped solid surface at the bottom of the indentation is referred to as the “bottom surface,” Figure 1B.

The optical properties of the shuriken TPS, immersed in buffer solution, as a function of nominal film thickness were characterized through the collection of reflectivity and optical rotatory dispersion (ORD) spectra, Figure 2. Both reflectivity and ORD spectra were collected with light polarized along the “short-axis” of the shuriken which is shown in Figure 2. As expected ORD spectra for left and right handed structures are mirror images of each other for all Au thicknesses; left and right handed structures display similar reflectance spectra. Both reflectivity and ORD measurements show a strong dependency on film thickness. The thickness dependency of the ORD spectra is qualitatively reproduced by EM modeling, Figure 3, with a slight blue shift, attributed to rounding of edges and inhomogeneity in experimental samples. The models show strong field enhancements at the edges of the shuriken nanostructure as well as surface plasmon polaritons (SPP) generated by the structures on the surface of the film.^[27,28]

These changes in optical properties can all be understood in terms of the increasing strength of the coupling (hybridization)

between electric and magnetic modes as the spatial overlap of the solid and inverse structures increases with film thickness. In the subsequent discussion we use the approach of Hentschel et al.^[24] to visualize the coupling of magnetic and electric modes within a hybrid system solely in terms of electric fields.

The dips observed in reflectance spectra collected for Au films of nominal thickness ≤ 30 nm have a characteristic asymmetric line shape of a Fano resonance,^[29,30] which in plasmonic systems arises through coupling between a “continuum state,” a broad optically bright mode, and a “discrete state,” a narrow dark mode (see the Supporting Information).^[31] EM modeling of the electric and magnetic field in the vicinity of the 30 nm structure, Figure 3G,H (additional plots in the Supporting Information), show different spatial distributions on the top and bottom surfaces. Overlap between the electric and magnetic fields of the top and bottom surface are not maximized, thus coupling between the inverse and solid structures is not optimal. It should be noted that due to its reduced thickness, the SPP propagate on both sides of the 30 nm film and evanescent fields are visible in the dielectric surrounding the solid structure and are to be ignored for this discussion.^[32,33] As the thickness is increased further (≥ 40 nm), a significant change in the reflectance dip occurs. A

peak of enhanced reflectivity begins to develop within the dip, becoming more pronounced with increasing film thickness. Peaks of enhanced reflectivity within reflectance dips have been observed previously in hybrid solid-inverse plasmonic structures;^[24] attributed to an electromagnetically induced transmission (EIT)-like phenomena. The origin of this EIT-like effect is due to strong coupling between bright and dark modes of the hybrid structure. For the 100 nm structure, Figure 3E,F, the electric fields associated with the top and bottom surface have matching spatial distributions but are out of phase; while the corresponding magnetic fields also have identical distributions and are in-phase, indicative of optimal coupling.

In the case of our chiral structures, the film thickness dependence of the coupling behavior has implications that extend beyond their reflectivity characteristics. Significant changes in ORD spectra occur concurrently with those observed in reflectance and further analysis of this behavior provides an insight into how the coupling between the two solid and inverse components alters with increasing film thickness, and how this changes the nature of the chirality. Using the analogy of natural optical activity occurring in molecules, it is useful to classify chromophores showing natural optical activity in terms of two limiting types:^[34] the inherently chiral chromophore in which the electronic states are delocalized over a chiral nuclear framework so that parallel components of electric and magnetic dipole moments are fully allowed for all transitions and which

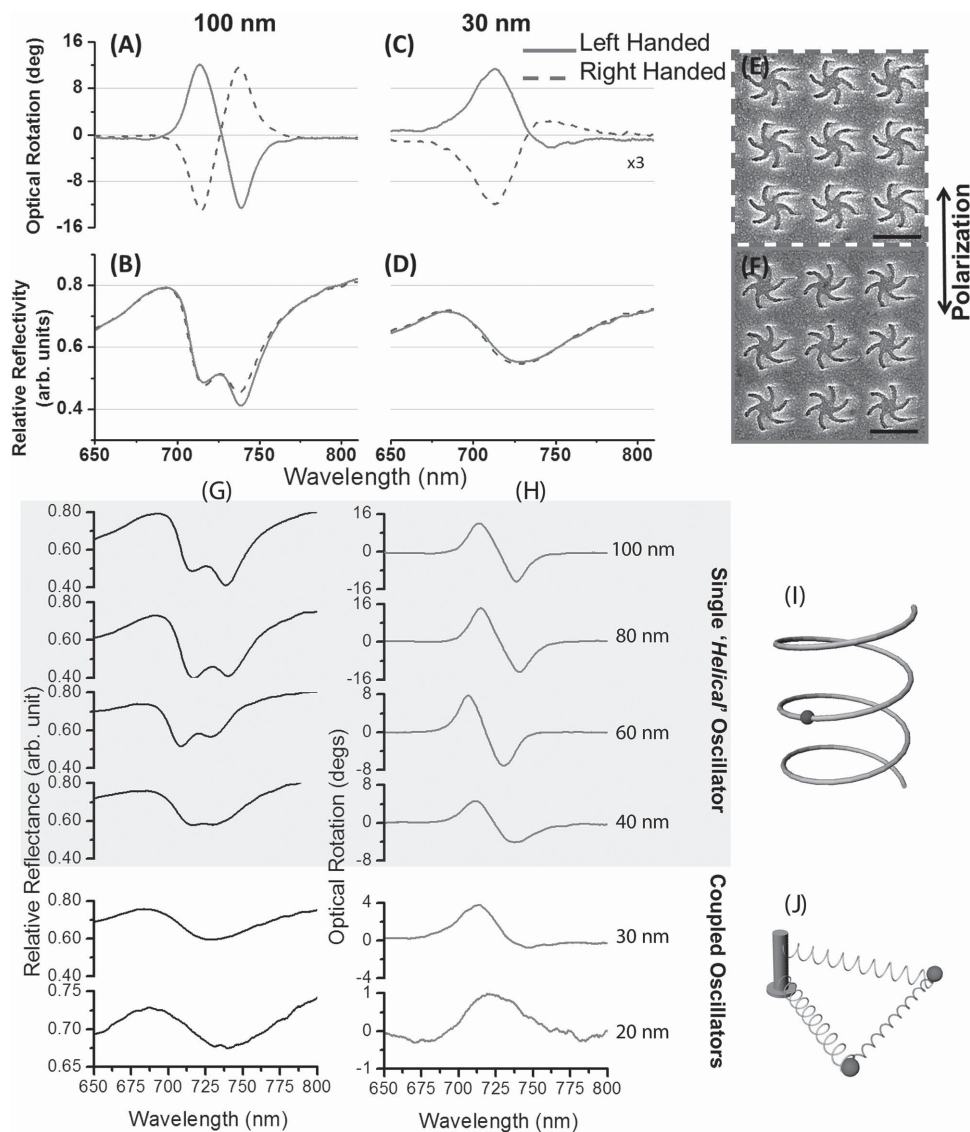


Figure 2. Experimental ORD and reflectivity measurements for right-handed (dashed line) and left handed (solid line) chiral “Shuriken” structures on (A,B) 100 nm and (C,D) 30 nm TPSs. SEM images of (E) right and (F) left handed structures with scale bars showing 500 nm. The ORD spectra for the 30 nm structures (C) have been multiplied by a factor of 3 for clarity. Column (G) show reflectivity spectra and column (H) shows ORD spectra collected from LH TPSs of varying nominal Au thickness. The reflectance is measured relative to an unstructured Au film of identical thickness. The TPS show either SHO type (I) or Born-Kuhn type (J) chirality.

may be pictured as a single helical oscillator (SHO); and the inherently achiral chromophore where coupling with the chiral environment is required. Two distinct coupling mechanisms can be distinguished.^[35] The “static coupling” mechanism invokes mixing of the electric and magnetic dipole transition moments on the same inherently achiral chromophore due to perturbations from the electrostatic fields of other groups in its chiral environment; and the “dynamic coupling” or “coupled oscillator” mechanism where the perturbations are due to electrodynamic fields radiated by other groups under the influence of the light wave and which becomes an “exciton” model in the case of degenerate transitions on two identical chromophores. ORD spectra from TPSs of 20 and 30 nm nominal Au thicknesses display the characteristic line shape associated with

dynamic coupling^[35] and might be described by a plasmonic realization of the Born-Kuhn (coupled oscillator, Figure 2J) model;^[36] whereas those from TPSs ≥ 40 nm display the line shape associated with static coupling^[35] (Figure 2I) which is also expected for an inherently chiral chromophore (SHO), the latter being more likely due to the large increase in the corresponding ORD signal, a typical property of inherently chiral chromophores. This difference in line shape implies that with increasing film thickness, there is a switch from an interaction between two or more dynamically coupled electric dipole transition moments to an interaction between spatially overlapping electric and magnetic dipole transition moments.

The thickness dependency of the optical properties of the TPS structures can be understood in terms of increasing

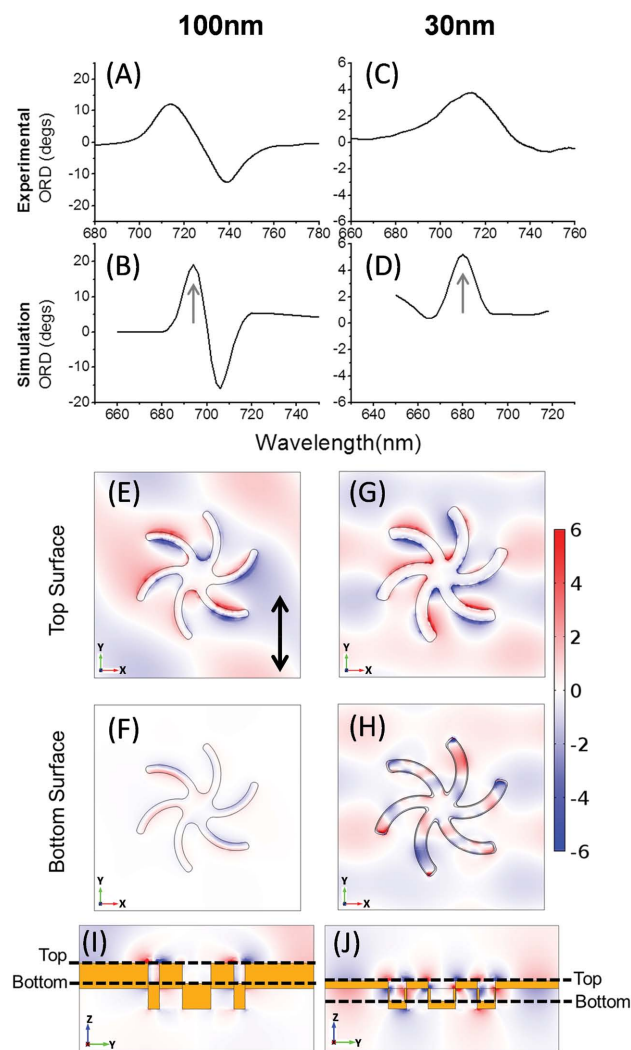


Figure 3. EM modeling results of 100 nm (left column) and 30 nm (right column) Au deposited structures are shown with experimental spectra for comparison. A,C) The experimental ORD spectra. B,D) The respective simulated spectra. The arrows in (B) and (D) show the wavelength at which the surface plots (E–H) of the z -component of the E -field density were generated. The black arrow in (E) shows the polarization of the incident E field for all simulation results. The E -field values on the color bar have the units MV m^{-1} . I,J) The side plots of a plane cutting through the two opposite arms. The black dashed lines show where the top surface and bottom surface lie. Surface plot (J) shows the model for 30 nm Au deposition with side walls connecting the inverse and solid structure to simulate a continuous film.

hybridization between magnetic and electric modes, with spatial overlap between the two. To provide a qualitative understanding of the coupling between the electric and magnetic modes of the solid and inverse structures a hybridization scheme, analogous to a molecular orbital diagram, can be constructed, **Figure 4**.^[23,37] As with molecular orbital diagrams, the first step in developing a hybridization scheme is to perform a symmetry analysis of the electric and magnetic modes of the shuriken solid and inverse structures. The shuriken belongs to the C_6 point group, hence the electric modes of the solid structure, and the symmetry identical magnetic modes of the inverse

structure, belong to A, B, E_1 , and E_2 symmetry species (symmetry arguments are based on information provided by the C_6 character table in the Supporting Information). Modes with A and E_1 symmetry are optically bright since they have dipolar character; but only the E_1 mode is accessible in the normal incident experimental geometry used, since the A mode can only be excited by vertical components of the exciting field (E_z or B_z). The EM modeling reiterates the excitation of an E_1 mode as the E fields of both structures, **Figure 3**, show an inversion in polarity for a C_2 rotation (refer to **Figure S7** and symmetry character table in the Supporting Information). The lowest energy dark mode is the E_2 mode which has a quadrupolar character; the B mode is also dark but is a higher order multipole and will have a higher energy. Since they have equivalent symmetry the electric dipole (quadrupole) and magnetic dipole (quadrupole) modes of the solid and inverse structures can hybridize. This produces new hybrid modes, which using the labeling of molecular orbitals, can be referred to as in- and out-of-phase modes, the former having the lowest energy. The in-phase out-of-phase combinations for the dipole hybrid modes are labeled D_{E+M} and D_{E-M} , respectively; while for the hybrid quadrupole modes they are Q_{E+M} and Q_{E-M} . The level of hybridization, and hence splitting of the in- and out-of-phase modes, increases with spatial overlap. Since the dipole-dipole and quadrupole-quadrupole interactions have r^{-3} and r^{-5} dependencies, increasing spatial overlap will cause a larger splitting of the Q_{E-M} and Q_{E+M} than the D_{E-M} and D_{E+M} levels, **Figure 4**. The ORD and reflectivity peaks we observe are associated with the out-of-phase D_{E-M} “bright” mode. This assignment is consistent as the EM modeling of both structures, **Figure 3**, show antiphase electric field patterns observed on the upper and lower surface for an excitable mode that correspond to an E_1 symmetry. The optical properties of the substrate could be influenced by the periodic arrangement of nanostructures. A square lattice belongs to the C_4 point group, but the presence of the shurikens reduces the symmetry of the extended lattice to C_2 . In a C_2 point group, all modes of the structure would be dipole active (bright) and consequently a Fano resonance would not be possible. Our observations suggest that in our structure, the lattice symmetry does not significantly influence the chiroptical properties, which are solely governed by the nanostructure symmetry.

The change from the Born-Kuhn to SHO chirality is inherent in the hybridization model as greater spatial overlap implies larger level of mixing of the magnetic and electric modes. The transition to EIT behavior, and thus the implicit increase in overlap between bright and dark modes, can also be understood in terms of the hybridization scheme. The energy separation, Δ , between the bright (D_{E-M}) and the dark (Q_{E+M}) modes decreases with increasing spatial overlap, thus resulting in greater coupling between the two.

To demonstrate the potential applications of the “disposable” TPSs we have used them to detect the secondary structure of a protein using a form of plasmonic polarimetry. Scattering of light near chiral nanostructures generates superchiral evanescent fields, the handedness of which depends on the handedness of the structure.^[5] These superchiral fields are sensitive to the protein structure. The origin of this sensitivity lies in the fact that a chiral molecule absorbs the superchiral evanescent fields based on the handedness of the field hence

Hybridization Scheme

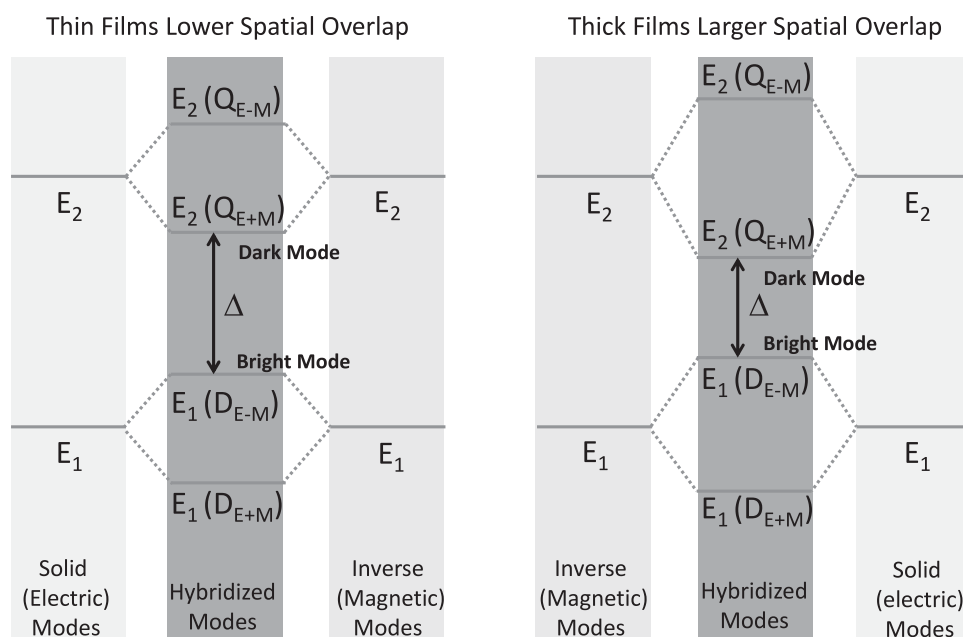


Figure 4. A scheme showing qualitative changes in the hybridization of electric and magnetic modes with increasing film thickness, and hence spatial overlap. Δ is the energy separation between the bright and the dark modes.

the refractive index for each handedness is different. As such, the resonance shift varies between the LH and RH structures providing us with two different values for the resonance shifts. The difference between the two shifts provides us with an asymmetry of the effective refractive index. This observed asymmetry is dependent on the protein secondary structure.^[5] In plasmonic polarimetry, shifts induced in the plasmonic resonances by the adsorption of a protein on LH and RH ($\Delta\lambda_L$ and $\Delta\lambda_R$) chiral nanostructures are measured. $\Delta\lambda_L$ and $\Delta\lambda_R$ are proportional to the refractive indices of the adsorbed proteins.^[38] The difference in the refractive index of an adsorbed material (protein) in LH and RH chiral evanescent fields is parametrized by a dissymmetry factor ($\Delta\Delta\lambda$), Equation (1):

$$\Delta\Delta\lambda = \Delta\lambda_R - \Delta\lambda_L \quad (1)$$

The $\Delta\Delta\lambda$ parameter is directly equivalent to optical rotation measured in traditional optical polarimetry.^[35] Achiral media will have identical refractive indices in left and right handed evanescent fields; hence $\Delta\lambda_L$ and $\Delta\lambda_R$ will be identical and $\Delta\Delta\lambda$ will be a zero value. We have performed calibration measurements to show this (the Supporting Information).

Plasmonic polarimetry measurements were made with 100 and 30 nm TPSs for a high β -sheet content protein Concanavalin A (Con A), **Figure 5A,B**. The amount of Con A detected in the experiment is ≈ 251 pg, estimated from calibration using surface plasmon resonance measurements on an unstructured Au surface. An overlap, between parallel electric and magnetic fields, leads to evanescent EM fields which possess a chiral asymmetry.^[39,40] Given the 100 nm TPS possess EM fields with the highest level of chiral asymmetry, **Figure 5C,D**

(see the Supporting Information), they are the most effective substrates to date for plasmonic polarimetry measurements, with $\Delta\Delta\lambda$ values for 30 and 100 nm TPS are 0.2 ± 0.4 and 1.9 ± 0.2 nm, respectively. Polyamino acids are a useful comparison to proteins which are made up of chains of amino acids (polypeptides). However unlike proteins, both enantiomers are available for polyamino acids. Therefore, we have performed plasmonic polarimetry measurements using 100 nm TPS, on L-, D-, and DL-(racemic) polylysine layers of approximately ≈ 1 nm thickness (see the Supporting Information). As expected, L- and D-layers, within experimental error, show equal and opposite ($\Delta\Delta\lambda$) values. The thinner polylysine films, 1 nm, show smaller asymmetries (-0.5 nm (L-) and 0.6 nm (D-)) compared to the thicker protein layers, ≈ 10 nm, as would be expected since they will cover a smaller region of the evanescent fields generated at the surface.

Using a novel hybrid inverse-solid plasmonic metafilm templated on a polycarbonate substrate, TPSs, we have demonstrated that near and far field chiral properties can be tuned using only film thickness. Varying film thickness, and hence spatial overlap, allows the hybridization between electric and magnetic modes of the solid and inverse structures to be controlled, thus enabling the chiroptical and EIT properties of the metafilm to be manipulated. Consequently, our work suggests that by designing structures with maximized hybridization between magnetic and electric modes, to thus mimic SHO type behavior, leads to metamaterials with enhanced chiroptical properties. Using an easily adjustable parameter such as Au film thickness provides a highly flexible paradigm to manipulate the hybridization of electric and magnetic modes within a (hybrid) metamaterial, compared to the current use of

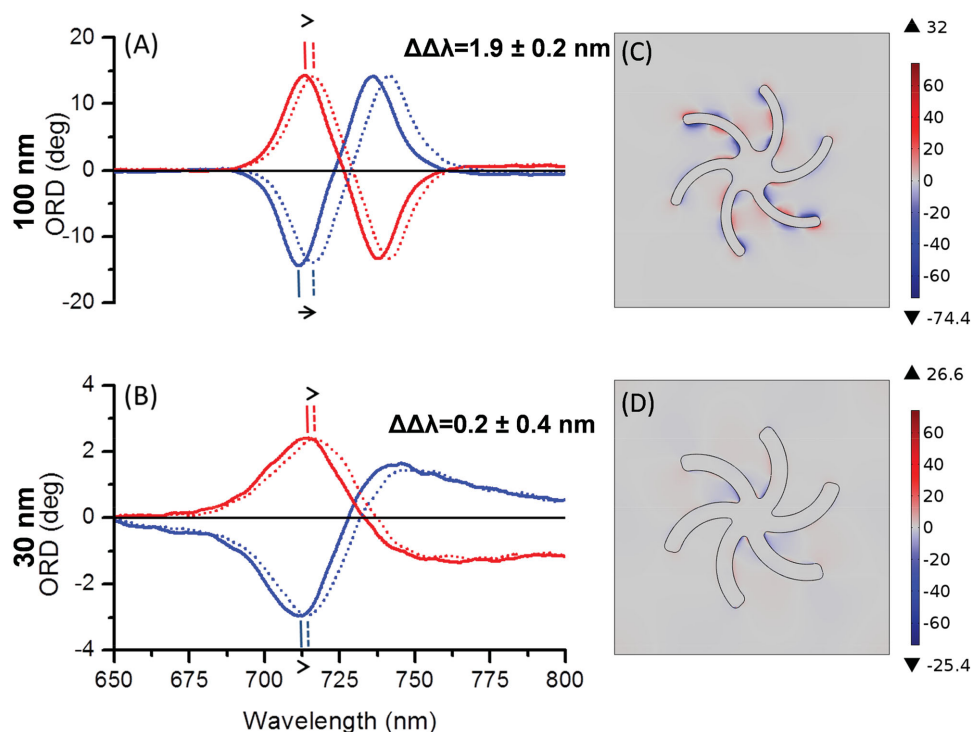


Figure 5. ORD spectra A) for 100 nm Au and B) for 30 nm TPSs. The red lines represent measurements on left handed TPS and blue represent measurement on right handed TPS. Spectra collected in the presence of buffer solution (solid lines) and Concanavalin A solution (dotted lines) shown. The vertical bars show the position of measurement of the particular peak in consideration. The arrows indicate direction of shift with the tail length giving an approximate comparison of the amount of shift. The corresponding $\Delta\Delta\lambda$ values are given. Maps of the optical chirality parameter derived from modeling for: C) the 100 nm and D) 30 nm TPSs are shown for wavelengths marked in Figure 3. The maps show the chiral fields on the Au surfaces of the top surface and the bottom surface (overlaid). The chirality values have been normalized to those of circularly polarized light. The maximum and minimum values for optical chirality are shown at the top and bottom ends of the color legends.

geometric structure driven control. When the flexibility of film thickness controlled coupling (hybridization) is combined with the cheap high throughput template polycarbonate substrates, we have a platform which brings the commercial exploitation of metamaterials, in areas such as biosensing, ever nearer.

Experimental Section

Fabrication: The TPS are created using injection molding of polycarbonate with a master Ni inlay. First, the desired nanopattern is fabricated using e-beam lithography. An electron beam writer (VB6, VISTEC) operated at 100 kV was used to generate the master on a Si substrate coated with 100 nm of PMMA resist. After development in a solution of isopropyl alcohol and methyl isobutyl ketone (3:1 ratio, Sigma-Aldrich), the surface topography is transferred to a Ni shim by electroplating. The polymer samples are then created by injection molding using an injection molder (Victory 28, Engel GmbH) using the Ni shim. The polymer substrates with nanopatterned surfaces are then coated with Au (MEB-400s, Plassys) by evaporation without the need of any metal adhesion layer. More details of the injection molding can be found in work by Stormonth-Darling et al.^[26] The Au coated substrates are cleaned in an oxygen plasma asher before measurements.

Optical Rotatory Dispersion (ORD) and Reflectivity Measurements: A custom made polarimeter has been developed that measures the reflected light from our samples. The design is similar to a basic reflected light microscope with a tungsten halogen light source (Thorlabs), Glan-Thompson polarizers (Thorlabs), and a 10 \times objective (Olympus, 0.16

NA). The samples are positioned with the help of a camera (Thorlabs) and the spectrum is measured using a compact spectrometer (Ocean optics USB4000). Using Stokes' methods, we can measure the intensity of light at four angles of the analyzer and calculate the optical rotation dispersion of our chiral plasmonic arrays.

Protein Measurements: The TPS were covered with a glass slide, with silicone for adhesion, to create a fluidic cell. Tris/HCl (10×10^{-3} M) buffer (Sigma-Aldrich) was used at pH 7.4 for buffer measurements before introducing a Concanavalin A solution into the cell which was left in for an hour before measuring for adsorbed proteins. Concanavalin A (ConA, Sigma-Aldrich) was prepared in solutions (1 mg mL^{-1}) using Tris/HCl (10×10^{-3} M) buffer at pH 7.4.

EM Simulations: COMSOL finite element modeling was used for simulating electromagnetic fields and ORD spectra of the structures. Floquet Periodic conditions were applied and normally incident linearly polarized (electric field along Y-component) light was used as the source. The refractive index values for Au were taken from a report by Johnson and Christy.^[41] The ORD has been calculated using the far field electric field components. The actual structural geometry is difficult to imitate as it varies with the amount of Au deposition. This has been catered for by varying geometry to fit the SEM evaluated geometry of the samples. More information is provided in the Supporting Information.

Supporting Information

Supporting Information is available from the Wiley Online Library or from the author.

Acknowledgements

The authors acknowledge financial support from the Engineering and Physical Sciences Research Council (EPSRC Grant No. EP/K034946), National Science Foundation (NSF Grant No. CHE-1307021), JSPS Core to Core programme, and A.S.K. thanks the Leverhulme Trust. R.T. and C.J. thank the EPSRC for the award of scholarships. They would also like to thank the technical support from the James Watt Nanofabrication Centre (JWNC). The authors would also like to acknowledge A. E. Kadodwala for instrument software development, as well as Shun Hashiyada and Dr. David France for useful discussions.

Received: April 16, 2015

Revised: July 2, 2015

Published online: August 26, 2015

- [1] J. N. J. Anker, W. P. Hall, O. Lyandres, N. N. C. Shah, J. Zhao, R. P. Van Duyne, *Nat. Mater.* **2008**, 7, 8.
- [2] J. K. Gansel, M. Thiel, M. S. Rill, M. Decker, K. Bade, V. Saile, G. von Freymann, S. Linden, M. Wegener, *Science* **2009**, 325, 1513.
- [3] J. B. Pendry, *Science* **2004**, 306, 1353.
- [4] V. M. Shalaev, *Nat. Photonics* **2007**, 1, 41.
- [5] E. Hendry, T. Carpy, J. Johnston, M. Popland, R. V. Mikhaylovskiy, A. J. Lapthorn, S. M. Kelly, L. D. Barron, N. Gadegaard, M. Kadodwala, *Nat. Nanotechnol.* **2010**, 5, 783.
- [6] E. Hutter, J. H. Fendler, *Adv. Mater.* **2004**, 16, 1685.
- [7] J. R. L. Guerreiro, M. Frederiksen, V. E. Bochenkov, V. De Freitas, M. G. Ferreira Sales, D. S. Sutherland, *ACS Nano* **2014**, 8, 7958.
- [8] P. K. Jain, X. Huang, I. H. El-Sayed, M. A. El-Sayed, *Plasmonics* **2007**, 2, 107.
- [9] K. L. Tsakmakidis, A. D. Boardman, O. Hess, *Nature* **2007**, 450, 397.
- [10] A. Vora, J. Gwamuri, N. Pala, A. Kulkarni, J. M. Pearce, D. Ö. Güney, *Sci. Rep.* **2014**, 4, 4901.
- [11] K. A. Willets, R. P. Van Duyne, *Annu. Rev. Phys. Chem.* **2007**, 58, 267.
- [12] X. Huang, P. K. Jain, I. H. El-Sayed, M. A. El-Sayed, *Lasers Med. Sci.* **2008**, 23, 217.
- [13] N. Liu, M. Hentschel, T. Weiss, A. P. Alivisatos, H. Giessen, *Science* **2011**, 332, 1407.
- [14] V. I. Belotelov, L. E. Kreilkamp, I. A. Akimov, A. N. Kalish, D. A. Bykov, S. Kature, V. J. Yallapragada, A. Venu Gopal, A. M. Grishin, S. I. Khartsev, M. Nur-E-Alam, M. Vasiliev, L. L. Doskolovich, D. R. Yakovlev, K. Alameh, A. K. Zvezdin, M. Bayer, *Nat. Commun.* **2013**, 4, 1.
- [15] T. Cao, C. Wei, R. E. Simpson, L. Zhang, M. J. Cryan, *Sci. Rep.* **2014**, 4, 4463.
- [16] M. Matschuk, N. B. Larsen, *J. Micromech. Microeng.* **2013**, 23, 025003.
- [17] K. Monkkonen, T. T. Pakkanen, J. Hietala, E. J. Paakkonen, P. Paakkonen, T. Jaaskelainen, T. Kaikuranta, *Polym. Eng. Sci.* **2002**, 42, 1600.
- [18] H. Sun, *Microsyst. Technol.* **2014**, 21, 1.
- [19] H. Pranov, H. K. Rasmussen, N. B. Larsen, N. Gadegaard, *Polym. Eng. Sci.* **2006**, 46, 160.
- [20] Y. Chen, J. Tao, X. Zhao, Z. Cui, A. S. Schwanecke, N. I. Zheludev, *Microelectron. Eng.* **2005**, 78–79, 612.
- [21] A. C. Liou, R. H. Chen, *Int. J. Adv. Manuf. Technol.* **2006**, 28, 1097.
- [22] N. Gadegaard, M. J. Dalby, E. Martinez, K. Seunarine, M. O. Riehle, A. S. G. Curtis, C. D. W. Wilkinson, *Adv. Sci. Technol.* **2006**, 53, 107.
- [23] E. Prodan, C. Radloff, N. J. Halas, P. Nordlander, *Science* **2003**, 302, 419.
- [24] M. Hentschel, T. Weiss, S. Bagheri, H. Giessen, *Nano Lett.* **2013**, 13, 4428.
- [25] J. Greener, R. Wimberger-Friedl, *Precision Injection Molding: Process, Materials, and Applications*, Hanser, Cincinnati, OH, USA, **2006**.
- [26] J. M. Stormonth-Darling, R. H. Pedersen, C. How, N. Gadegaard, *J. Micromech. Microeng.* **2014**, 24, 075019.
- [27] P. Lalanne, J. P. Hugonin, J. C. Rodier, *Phys. Rev. Lett.* **2005**, 95, 1.
- [28] H. Liu, P. Lalanne, X. Yang, J. P. Hugonin, *IEEE J. Sel. Top. Quantum Electron.* **2008**, 14, 1522.
- [29] B. Luk'yanchuk, N. I. Zheludev, S. A. Maier, N. J. Halas, P. Nordlander, H. Giessen, C. T. Chong, *Nat. Mater.* **2010**, 9, 707.
- [30] B. Gallinet, A. Lovera, T. Siegfried, H. Sigg, O. J. F. Martin, *AIP Conf. Proc.* **2012**, 1475, 18.
- [31] V. Giannini, Y. Francescato, H. Amrania, C. C. Phillips, S. A. Maier, *Nano Lett.* **2011**, 11, 2835.
- [32] P. Berini, *Phys. Rev. B* **2000**, 61, 10484.
- [33] S. A. Maier, *Plasmonics: Fundamentals and Applications*, Springer, New York, **2007**.
- [34] C. W. Deutsche, D. A. Lightner, R. W. Woody, A. Moscovitz, *Annu. Rev. Phys. Chem.* **1969**, 20, 407.
- [35] L. D. Barron, *Molecular Light Scattering and Optical Activity*, Cambridge University Press, New York **2009**.
- [36] X. Yin, M. Schäferling, B. Metzger, H. Giessen, *Nano Lett.* **2013**, 13, 6238.
- [37] P. W. Atkins, R. S. Friedman, *Molecular Quantum Mechanics: An Introduction to Quantum Chemistry*, Oxford University Press, New York **2011**.
- [38] J. Anker, W. Hall, O. Lyandres, N. Shah, *Nat. Mater.* **2008**, 7, 8.
- [39] V. K. Valev, J. J. Baumberg, C. Sibilia, T. Verbiest, *Adv. Mater.* **2013**, 25, 2517.
- [40] E. Hendry, R. V. Mikhaylovskiy, L. D. Barron, M. Kadodwala, T. J. Davis, *Nano Lett.* **2012**, 12, 3640.
- [41] P. Johnson, R. Christy, *Phys. Rev. B* **1972**, 6, 4370.